ADVANCED ELECTRONIC MATERIALS

Supporting Information

for *Adv. Electron. Mater.,* DOI: 10.1002/aelm.202101286

Boosted Charge-Carrier Transport in Triple-Cation Perovskites by Ultrasonic Vibration Post Treatment

Yuzhuo Wang, Mohammad-Reza Ahmadian-Yazdi, Yangyang Ni, Yexin Jiang, Morteza Eslamian, Zuanming Jin, and Qianli Chen**

Supporting Information

Boosted Charge-Carrier Transport in Triple-Cation Perovskites by Ultrasonic Vibration Post Treatment

Yuzhuo Wang, Mohammad-Reza Ahmadian-Yazdi, Yangyang Ni, Yexin Jiang, Morteza Eslamian, Zuanming Jin, Qianli Chen**

1. Film thickness

The determined thicknesses for all samples were 280 ± 10 nm (Figure S1). In contrast to the finding in the previous work by Ahmadian-Yazdi et al.[1] in 2018, we concluded that the perovskite layer did not penetrate through ZIF-8 during vibration, since the perovskite film thickness did not decrease as the vibration time extended.

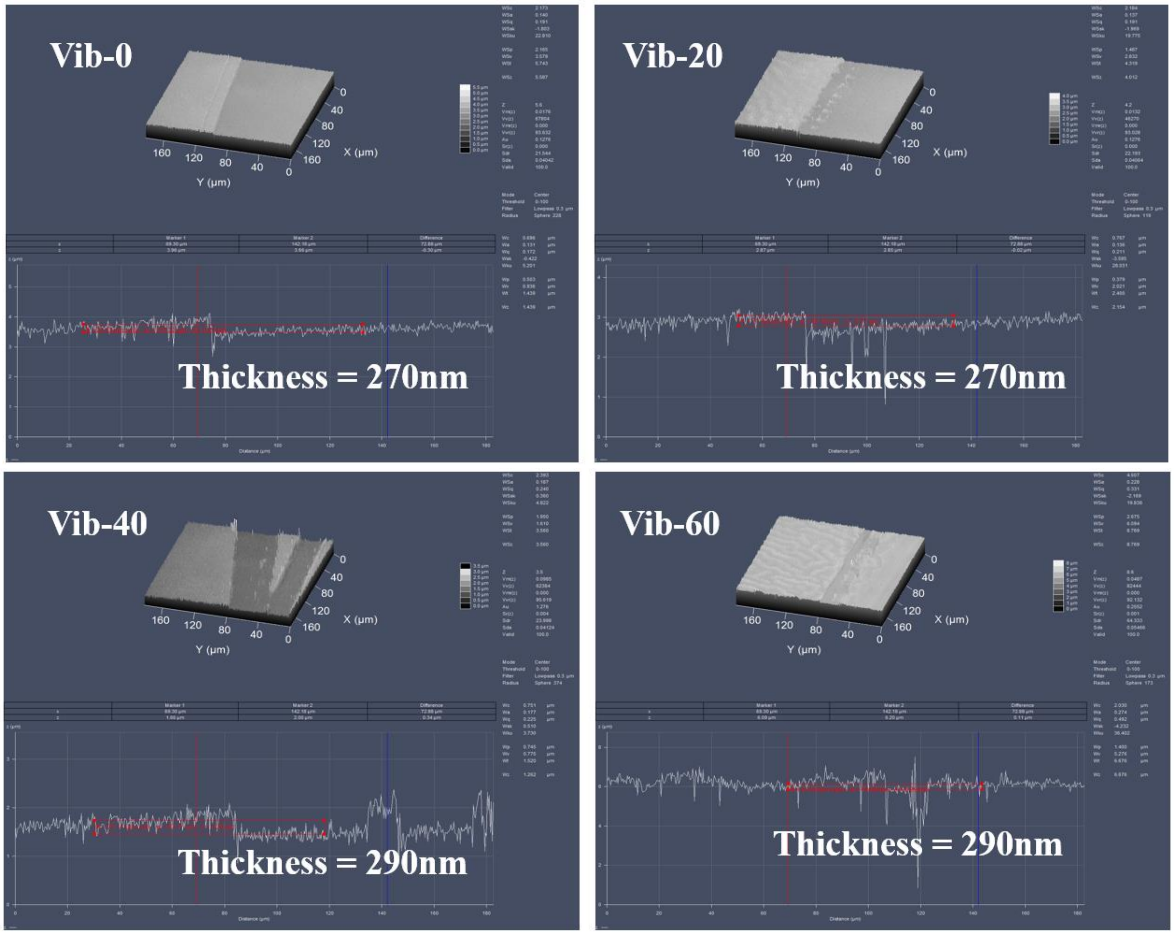

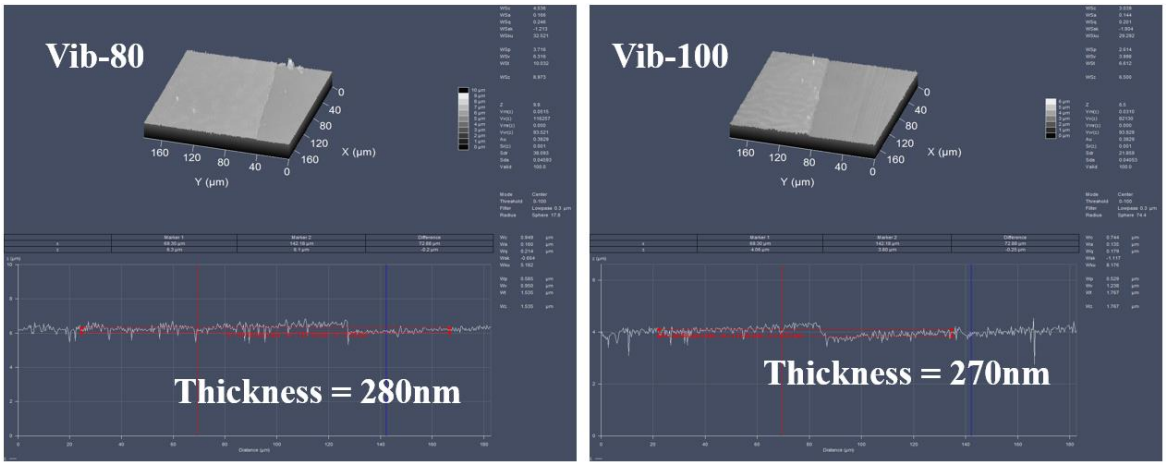

Figure S1. Surface profile of Vib-0 to 100 captured by a confocal laser scanning microscope, with thickness of perovskite layer marked on each image.

2. UV-Vis absorption spectra

UV-vis absorbance spectra of all samples were obtained in order to study compositional and structural properties of perovskites. For wavelength smaller than 450 nm, Vib-0, 20, 80 and 100 showed relatively high absorbance compared with Vib-40 and 60, indicating a more crystallized film and higher coverage on the substrate. This is also in agreement with our SEM results. Yet, for Vib-60, the height of platform for absorbance near 450 nm still exceeds that of Vib-40 even though the mean grain sizes of these two samples are statistically identical. When the wavelength is at 720 nm, an extraordinarily sharp cutoff is observed, representing a clear direct band structure.

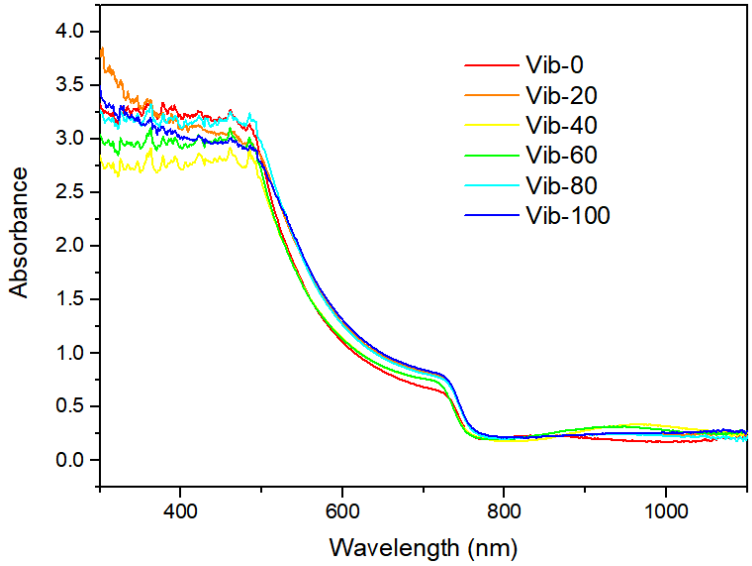

Figure S2. Absorbance spectra of samples Vib-0 to 100.

3. Band-gap determination

We further determined that the optical band gaps of our samples range from 1.64 to 1.66 eV from Tauc plots, as shown in Figure S3. The band gap values are consistent with previous reports.[2]

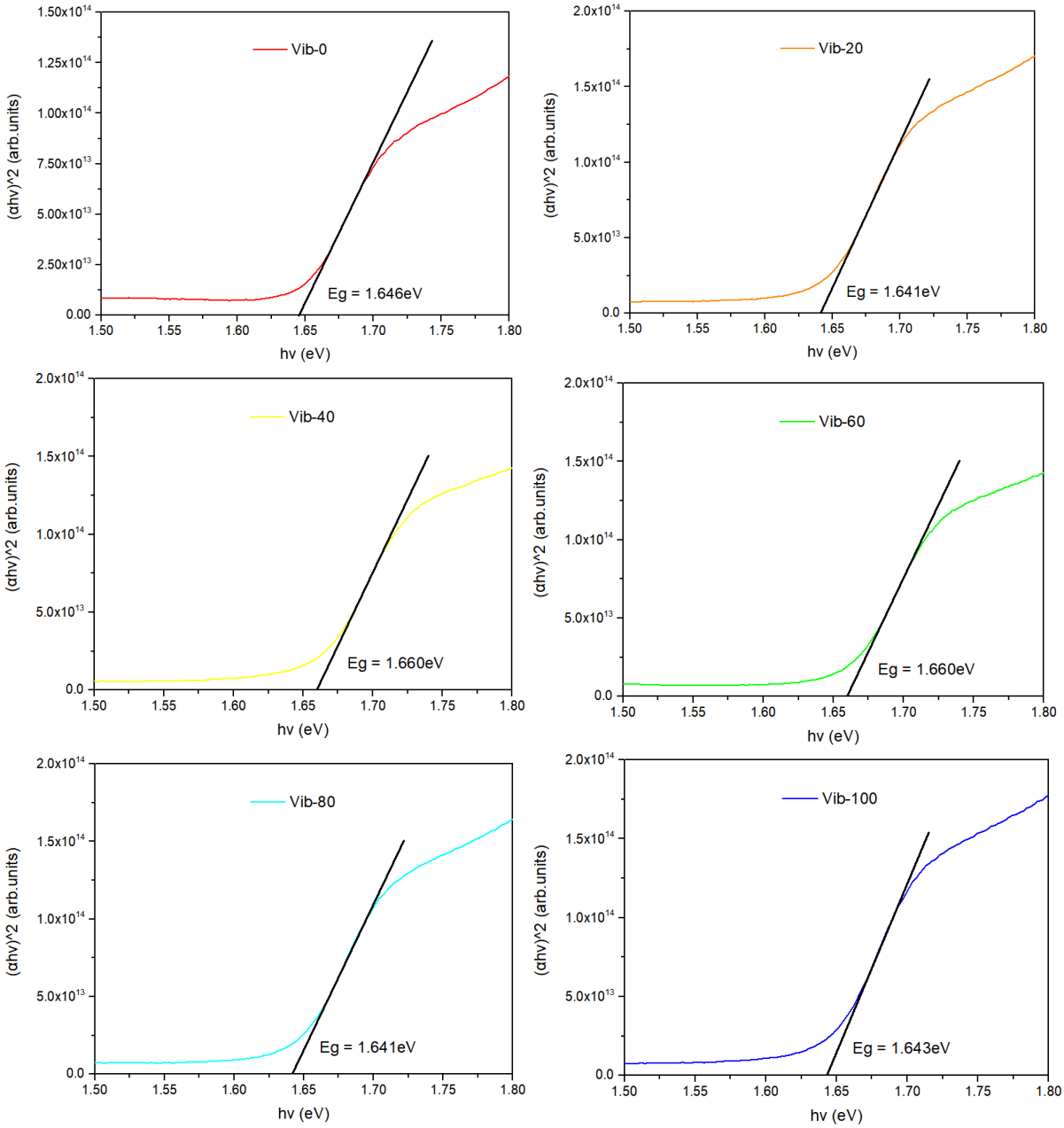

Figure S3. Band gap extracted from Tauc plots of Vib-0 to 100 based on UV-Vis results.

4. Additional PL, TRPL results and fitting details

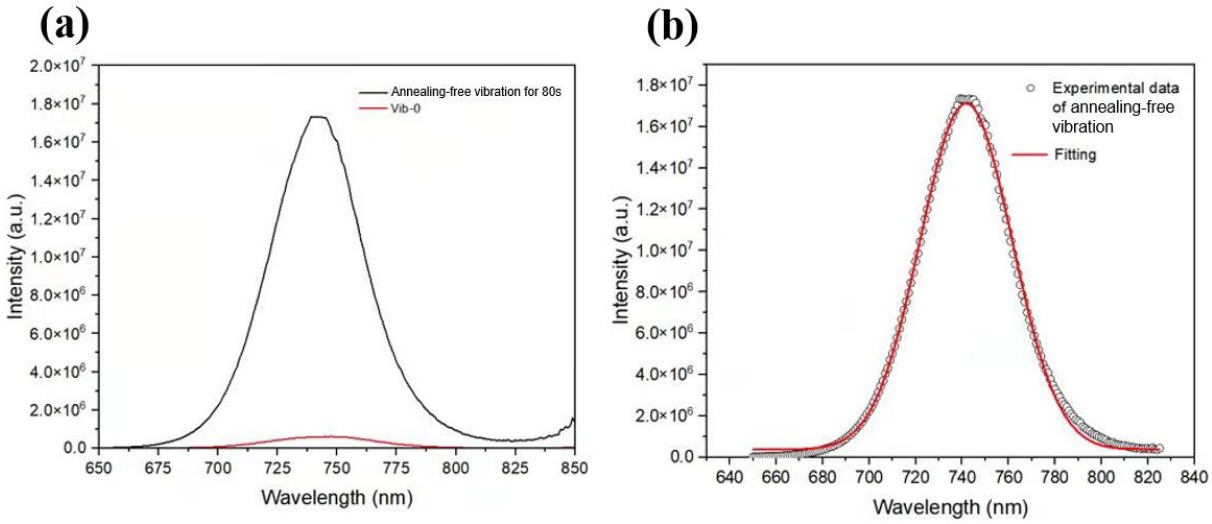

Figure S4. (a) Steady-state PL spectra of perovskite films processed with annealing-free vibration for 80 s and pure annealing for 45 minutes. To keep the PL intensity within the instrument measurement range, for annealing-free vibration film, the scan slit and fixed slit were reduced from 8 to 2 μm, and from 7 to 2 μm, respectively. (b) Single Gaussian curve fitting for PL spectrum of annealing-free vibration film.

5. Analysis of steady-state photoluminescence spectra

Here we note that the energy of the bandgap obtained from PL spectra is different from the stable optical gap, which could be explained by band filling.[2]

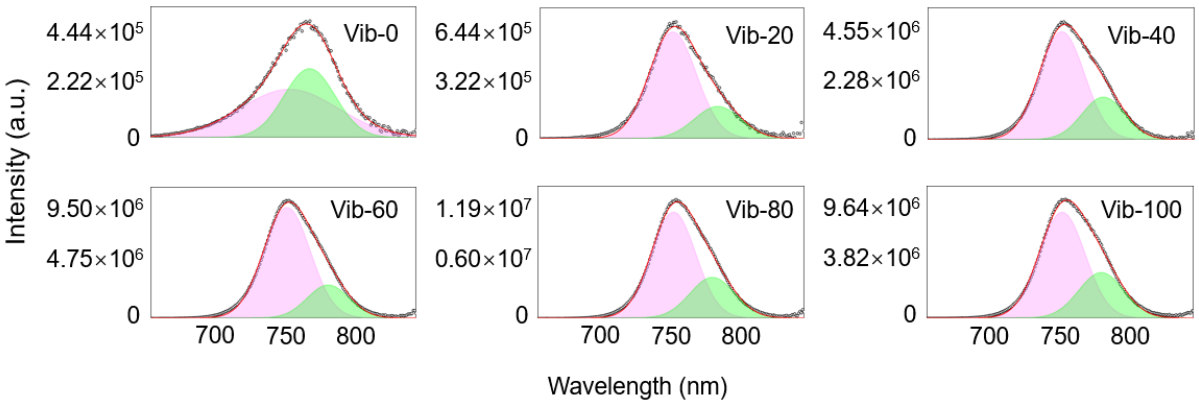

Figure S5. PL spectra of all films fitted by two Gaussian functions. The pink region denotes the emission of free excitons, the green region denotes the emission of trap states, while the red curve denotes the fitted result consisting of both Gaussian functions. All fitted curves showed goodness exceeding 99.8%.

6. Determination of photoconductivity

The photoconductivity $\sigma(t)$ is obtained by probing the relative change in the peak field of the THz pulse $-\Delta E(t)/E(t)$, using the following equation:

$$\sigma(t) = -\frac{(n_1 + n_2)}{Z_0 \cdot l} \cdot \frac{\Delta E(t)}{E(t)} \#(S1)$$

where $\Delta E(t) = E_{pump}(t) - E(t)$ is the pump-induced THz electric field changes, n_1 and n_2 denote the refractive indices of the media before and after the sample, where $n_1 = 1$ is for vacuum and $n_2 = 1.95$ is for z-cut quartz substrate. $Z_0 = 377\Omega$ is the impedance of free space, and $l = 280\ nm$ is the thickness of perovskite film. By applying the Fourier transform, we convert Equation S1 into:

$$\sigma(\omega) = -\frac{(n_1 + n_2)}{Z_0 \cdot l} \cdot \frac{\Delta E(\omega)}{E(\omega)} \#(S2)$$

Thus, we obtain the frequency resolved photoconductivity.

7. Determination of recombination rate constants

The recombination rate equation is described by the following relation:

$$\frac{dn(t)}{dt} = -k_3 n^3 - k_2 n^2 - k_1 n \#(S3)$$

where $n(t)$ denotes the time-dependent carrier density, k_1 denotes the monomolecular recombination rate constant arising from charge-carrier trapping; k_2 denotes the bimolecular recombination rate constant representing the free electron-hole pair recombination; k_3 represents the Auger recombination rate constant. In this study, k_1 was obtained by linear fitting at the tails of each TRPL curve, when this test is conducted at a low fluence condition so that only the monomolecular recombination process is triggered. The fitting details for TRPL are shown in Figure S6, and we therefore obtained $k_{1,Vib-0} = 13.892 \times 10^6\ s^{-1}$ and $k_{1,Vib-80} = 8.131 \times 10^6\ s^{-1}$.

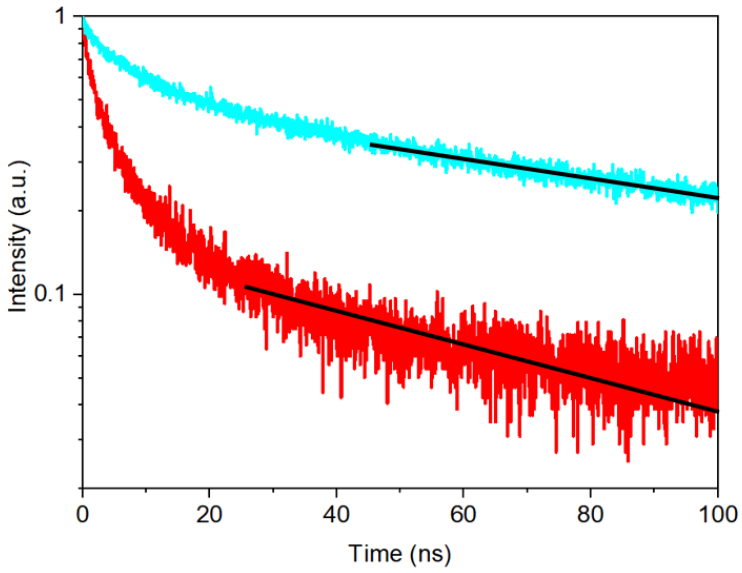

Figure S6. Time resolved photoluminescence spectroscopy of Vib-0 (red) and Vib-80 (cyan) at 400nm, with linear fitting regions marked.

The other two coefficients k_2 and k_3 were obtained from the fitting process of THz conductivity transients, using the k_1 obtained from TRPL, as was performed in the data analysis before.[3-5] Defining $x(t) = \left(\frac{\Delta T}{T}\right)(t)$ to replace the THz photoconductivity change, it is linearly related to the free charge carrier in form of:

$$n(t) = \varphi C x(t) \#(S4)$$

In Equation S4, $C = N_{abs}/x$ is a proportionality factor between the peak of THz response x and the initially absorbed photon density N_{abs}. φ is the ratio of charge carriers produced following photon absorption, also known as the photon-to-charge branching ratio. Since we cannot determine the value of φ directly, it is included in the results of k_2 and k_3 as bundled coefficients. $N_{Vib-0} = 9.8475 \times 10^{17}\text{cm}^{-3}$ and $N_{Vib-80} = 1.1768 \times 10^{18}\text{cm}^{-3}$ obtained from THz conductivity spectra were used in our calculation as charge carrier density. If Eq. S4 is substituted into Eq. S3, we obtain the following relation:

$$\frac{dx(t)}{dt} = -C^2\varphi^2 k_3 x^3 - C\varphi k_2 x^2 - k_1 x = -A_3 x^3 - A_2 x^2 - A_1 x \#(S5)$$

with $A_i = C^{i-1}\varphi^{i-1}k_i$. Applying a global fitting for all four fluences using Eq. S5, we obtain the following fitting curves in Figure 2 with all coefficients falling within the range of typical

values. We concluded that all three recombination coefficients were effectively suppressed with applying vibration.

8. Estimation of charge-carrier diffusion length

The charge-carrier diffusion length is calculated by:

$$L_D(n) = \sqrt{\frac{D}{R_{total}(n)}} \#(S6)$$

The total recombination rate $R_{total}(n)$ is determined by the charge carrier density and the recombination rate constants (k_1, k_2 and k_3) of the individual recombination process:

$$R_{total} = -\frac{1}{n}\frac{dn}{dt} = n^2 k_3 + n k_2 + k_1 \#(S7)$$

Here, the diffusion constant D is expressed by Einstein relation:

$$D = \frac{\mu k_B T}{e} \#(S8)$$

where $T = 291.55\ K$, $e = 1.6 \times 10^{-19}\ C$ and $k_B = 1.38 \times 10^{-23} J/K$. The relation of charge carrier diffusion length as a function of charge carrier concentration is shown for both Vib-0 and Vib-80 in Figure 4b.

Table S1. Detailed stats of triple-exponential fitting for TRPL results on Vib-0, 20, 40, 60, 80, 100.

Sample Name	A_1	τ_1(ns)	A_2	τ_2(ns)	A_3	τ_3(ns)	$\langle\tau_{avg}\rangle$ (ns)	Goodness of fit R^2
Vib-0	0.0886	179.7	0.4066	9.583	0.5048	1.205	20.42	0.9802
Vib-20	0.1002	107.4	0.3891	13.47	0.5107	2.464	17.26	0.9902
Vib-40	0.2698	87.67	0.4227	12.96	0.3075	2.050	29.76	0.9904
Vib-60	0.2677	103.0	0.4134	21.15	0.3189	3.187	37.33	0.9972
Vib-80	0.4410	151.0	0.3435	16.81	0.2155	1.882	72.77	0.9922
Vib-100	0.3161	109.1	0.3920	13.71	0.2919	2.090	40.47	0.9936
Annealing-free vibration	0.8834	2978	0.0842	36.08	0.0324	2.726	2634	0.8617

9. X-ray diffraction (XRD) patterns

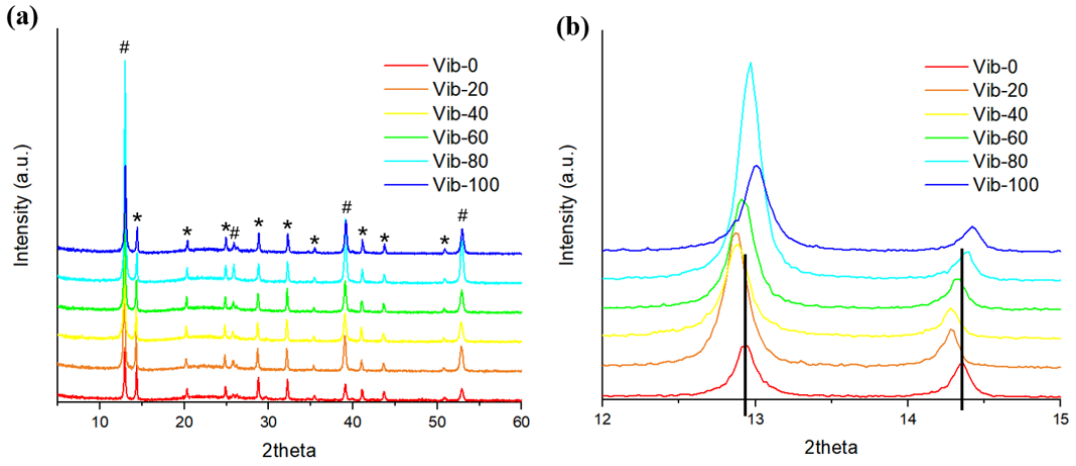

Figure S7. XRD patterns from Vib-0 to Vib-100. All * peaks denote perovskite structure, while the # peaks denote the residual PbI_2.

10. Surface morphology

We obtained surface morphology images with scanning electron spectroscopy (SEM) for Vib-0, 20, 40, 60, 80 and 100, as observed in Figure S9(a) to (f). All samples show uniformly distributed grains with distinguishable grain boundaries, and compact and pinhole-free surface. The mean grain size was obtained from Gaussian fitting on the size distribution diagrams. For each sample, the grain size was measured from the Feret diameters of grains by averaging 3 SEM images. For the ultrasonic vibration time between 0 and 80 s, the grain size variation is within their standard deviation, whereas the mean grain size for Vib-100 decreased by 30%. The vibration time-dependent mean grain size is shown in Figure S8(g). It's worth noting that a similar trend for grain size has been obtained in a previous report,[1] where the effect of ultrasonic vibration was studied on $MAPbI_3$ perovskite layer deposited on mesoporous-TiO_2.

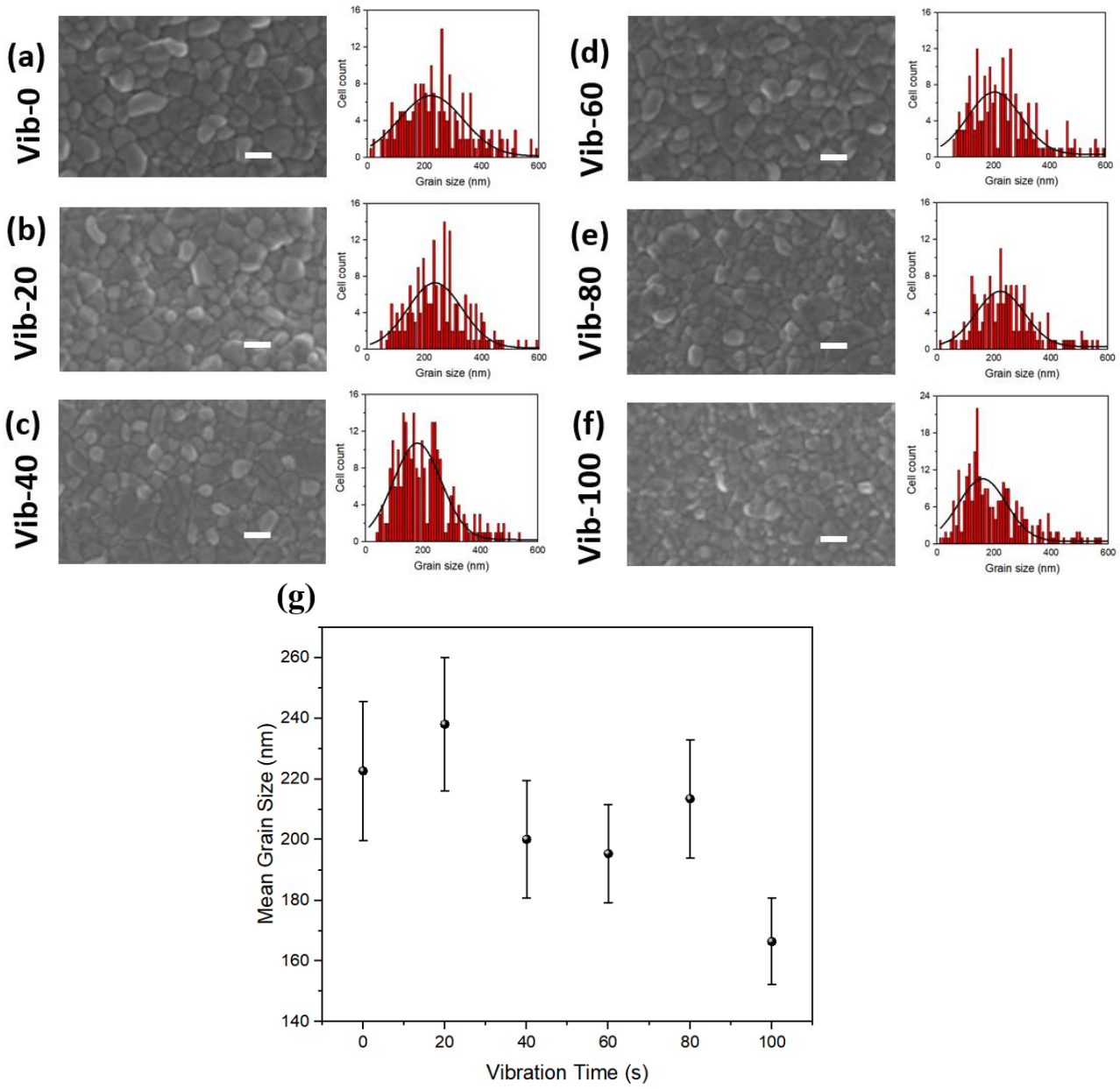

Figure S8. Top-down SEM images and the Gaussian distributions of grain size of perovskite films prepared on z-cut quartz substrates with (a) no vibration, and (b) 20 s, (c) 40 s, (d) 60 s, (e) 80 s, (f) 100 s of vibration treatment. All scale bars are 200 nm. (g) Mean grain size of perovskite films prepared on z-cut quartz substrates with various times of vibration treatment.

11. TRPL curves and fitting details for vibration time longer than 100s

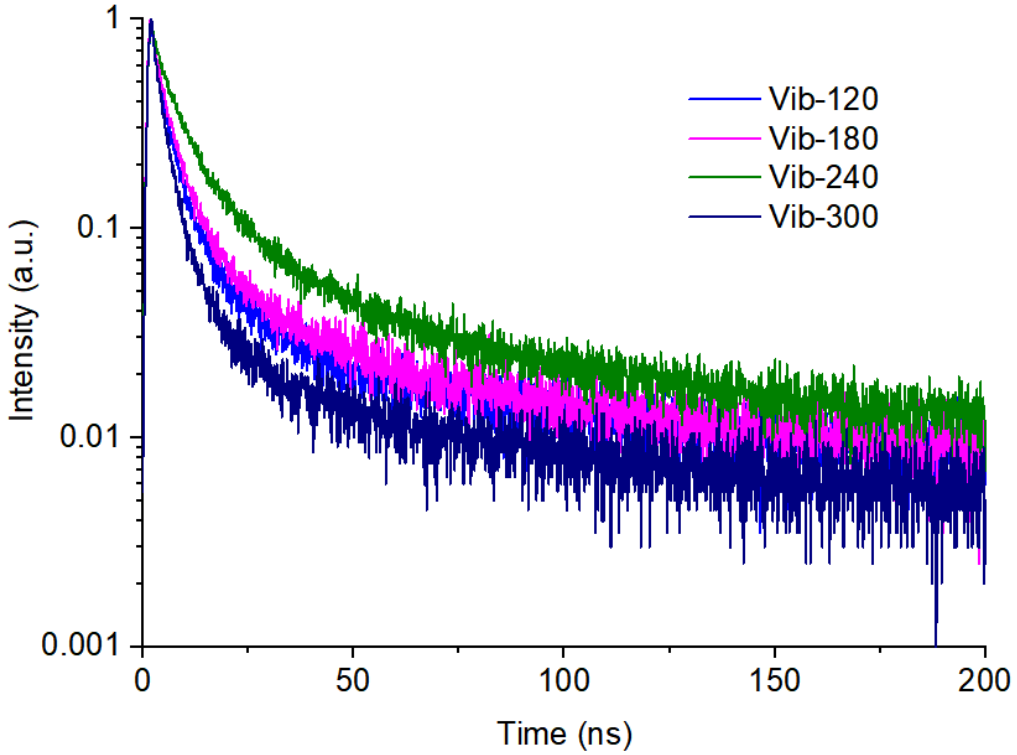

Figure S9. Normalized TRPL spectra of films Vib-120, 180, 240 and 300. All possessing charge-carrier lifetimes are < 25 ns.

Table S2. Detailed stats of triple-exponential fitting for TRPL results on Vib-120, 180, 240, 300.

Sample Name	A_1	τ_1(ns)	A_2	τ_2(ns)	A_3	τ_3(ns)	$\langle\tau_{avg}\rangle$ (ns)	Goodness of fit R^2
Vib-120	0.0327	123.5	0.4868	5.942	0.4805	1.486	7.646	0.9966
Vib-180	0.0424	101.9	0.5422	6.134	0.4154	1.532	8.287	0.9970
Vib-240	0.0678	97.21	0.6010	8.713	0.3312	1.640	12.37	0.9969
Vib-300	0.0206	123.9	0.3635	5.303	0.6159	1.748	5.559	0.9976

12. Comparison of charge-carrier mobility measured in this work with previous reports for other perovskite thin films

Table S3. Comparison of charge-carrier mobility measured in this work with previous reports for similar perovskite compositions measured using time-resolved THz spectroscopy.

Composition	Microstructure	Mobility ($cm^2V^{-1}s^{-1}$)	Reference
$Cs_{0.05}(MA_{0.17}FA_{0.83})_{0.95}Pb(I_{0.83}Br_{0.17})_3$	Polycrystalline thin film	121 **± 44**	This work
$MAPbI_3$	Polycrystalline thin film	33	[6]
$FAPbI_3$	Polycrystalline thin film	27	[4]
$Cs_{0.17}FA_{0.83}PbI_3$	Polycrystalline thin film	40	[7]
$Cs_{0.17}FA_{0.83}Pb(I_{0.6}Br_{0.4})_3$	Polycrystalline thin film	21	[8]
$Cs_{0.17}FA_{0.83}Pb(I_{0.8}Br_{0.2})_3$	Polycrystalline thin film	~23	[9]
$CsPbI_3$	Polycrystalline thin film	270 ± 44	[10]
$MAPbI_3$	single crystal	~620	[11]

References:

[1] Ahmadian-Yazdi, M.-R.; Habibi, M.; Eslamian, M. Excitation of Wet Perovskite Films by Ultrasonic Vibration Improves the Device Performance. Applied Sciences **2018**, 8 (2), 308.

[2] Fan, J.; Shavel, A.; Zamani, R.; Fábrega, C.; Rousset, J.; Haller, S.; Güell, F.; Carrete, A.; Andreu, T.; Arbiol, J.; Morante, J. R.; Cabot, A. Control of the Doping Concentration, Morphology and Optoelectronic Properties of Vertically Aligned Chlorine-Doped ZnO Nanowires. Acta Materialia **2011**, 59 (17), 6790–6800.

[3] C. Wehrenfennig, M. Liu, H. J. Snaith, M. B. Johnston, L. M. Herz, *Energy Environ. Sci.* **2014**, 7, 2269.

[4] W. Rehman, R. L. Milot, G. E. Eperon, C. Wehrenfennig, J. L. Boland, H. J. Snaith, M. B. Johnston, L. M. Herz, *Advanced Materials* **2015**, 27, 7938.

[5] R. L. Milot, G. E. Eperon, H. J. Smith, M. B. Johnston, L. M. Herz, *Advanced Functional Materials* **2015**, 25, 6218.

[6] C. Q. Xia, J. Peng, S. Poncé, J. B. Patel, A. D. Wright, T. W. Crothers, M. Uller Rothmann, J. Borchert, R. L. Milot, H. Kraus, Q. Lin, F. Giustino, L. M. Herz, M. B. Johnston, *The Journal of Physical Chemistry Letters* **2021**, 12, 3607.

[7] W. Rehman, D. P. McMeekin, J. B. Patel, R. L. Milot, M. B. Johnston, H. J. Snaith, L. M. Herz, *Energy & Environmental Science* **2017**, 10, 361.

[8] D. P. McMeekin, G. Sadoughi, W. Rehman, G. E. Eperon, M. Saliba, M. T. Hörantner, A. Haghighirad, N. Sakai, L. Korte, B. Rech, M. B. Johnston, L. M. Herz, H. J. Snaith, *Science* **2016**, 351, 151.

[9] D. P. McMeekin, Z. Wang, W. Rehman, F. Pulvirenti, J. B. Patel, N. K. Noel, M. B. Johnston, S. R. Marder, L. M. Herz, H. J. Snaith, *Advanced Materials* **2017**, 29, 1607039.

[10] H. Zhang, E. Debroye, J. A. Steele, M. B. Roeffaers, J. Hofkens, H. I. Wang, M. Bonn, *ACS Energy Letters* **2021**, 6, 568.

[11] D. A. Valverde-Chávez, C. S. Ponseca, C. C. Stoumpos, A. Yartsev, M. G. Kanatzidis, V. Sundström, D. G. Cooke, *Energy & Environmental Science* **2015**, 8, 3700.